



High resolution 3-D crustal structure beneath NE China from joint inversion of ambient noise and receiver functions using NECESSArray data



Zhen Guo^{a,g}, Y. John Chen^{a,*}, Jieyuan Ning^a, Yongge Feng^a, Stephen P. Grand^b, Fenglin Niu^c, Hitoshi Kawakatsu^d, Satoru Tanaka^e, Masayuki Obayashi^e, James Ni^f

^a Institute of Theoretical and Applied Geophysics, School of Earth and Space Sciences, Peking University, Beijing, China

^b Department of Geological Sciences, The University of Texas at Austin, Austin, TX, USA

^c Department of Earth Science, Rice University, Houston, TX, USA

^d Earthquake Research Institute, University of Tokyo, Tokyo, Japan

^e Department of Earth Structure and Dynamics Research, Japan Agency for Marine–Earth Science and Technology, Yokosuka, Japan

^f Department of Physics, New Mexico State University, Las Cruces, NM, USA

^g ARC Centre of Excellence for Core to Crust Fluid Systems and GEMOC ARC National Key Centre, Dept. Earth and Planetary Sciences, Macquarie University, North Ryde, NSW2109, Australia

ARTICLE INFO

Article history:

Received 8 September 2014

Received in revised form 29 January 2015

Accepted 31 January 2015

Available online xxxx

Editor: P. Shearer

Keywords:

joint inversion

receiver functions

ambient noise tomography

Songliao Basin

Xing'an–Mongolia Orogenic Belt

ABSTRACT

We used ambient noise data recorded by the NECESSArray, a portable seismic array deployed in Northeast China, to construct Rayleigh-wave phase velocity dispersion curves and obtain phase velocity maps for periods from 6 to 40 s. S-wave velocity structure beneath NE China is obtained by joint inversion of the phase velocities and receiver functions. Our results show good correlation between crustal velocity structure and geological features. At shallow depths the Songliao Basin is separated into two small sub-basins by a fast velocity anomaly corresponding to a southwest uplifted horst and the southern sub-basin is associated with the Kailu depression. A low-velocity anomaly extending from the lower-crust to uppermost mantle beneath the Changbaishan mountain range is consistent with P- and S-wave tomography models. The mantle low velocity has been interpreted as a local mantle upwelling attributed to the subducting Pacific slab induced return flow. Finally, the S-wave velocity in the mid-and-lower crust is lower beneath the Xing'an–Mongolia Orogenic Belt (XMOB) than beneath the Changbaishan mountain range. This was not expected since the Changbaishan mountain range has experienced more extensive volcanic activity in the Cenozoic, including the currently active Changbaishan and Jingpohu volcanoes, than the XMOB. We infer that the mid-and-lower crust of the XMOB is mainly felsic in composition and propose that the low shear-wave velocity of the mid-and-lower crust beneath the XMOB could be the consequence of removal of deep mafic crust through a continental accretion and subsequent delamination event in the Paleozoic, or via convection removal induced by the rollback of the flat subducted Paleo-Pacific slab during the middle Mesozoic.

© 2015 Published by Elsevier B.V.

1. Introduction

Northeast China (hereafter NE China) is a mosaic of several blocks in the Paleozoic subjected to serial episodes of continental accretions (Zhou and Wilde, 2013). Broadly, the region consists of three tectonic units including the Xing'an–Mongolia Orogenic Belt (XMOB) in the west, the Songliao basin (SLB) at the center, and the Changbaishan mountain range (CBM) in the east. NE China lies between the North China Craton (NCC) and the Siberian Cra-

ton, separated by the Solonker suture and the Mongol–Okhotsk suture, respectively. To the east is the Japan Trench where the Pacific oceanic plate is subducting beneath Eurasia. The Paleo-Asian Ocean closed along the Solonker suture in Late Triassic (~200 Ma) (Sengor et al., 1993; Xiao et al., 2003) and subsequent closure of the Mongol–Okhotsk Ocean along the Mongol–Okhotsk suture zone in the north during the Middle Jurassic (~160 Ma) completes the final amalgamation of NE China between Siberia and the NCC (Zhou and Wilde, 2013).

During the late Mesozoic, NE China experienced extensive volcanism and extension, probably related to the subduction of the Paleo-Pacific plate to the east and the closure of Mongol–Okhotsk sea to the north (Chen and Pei, 2010; Lei and Zhao, 2005; Liu

* Corresponding author. Tel.: +8613683583697.

E-mail address: johnyc@pku.edu.cn (Y.J. Chen).

et al., 2001; Meng, 2003; Wang et al., 2006; Wu et al., 2004). Rifting and crustal extension have led to the formation of several intra-continental extensional basins, including the Songliao basin (SLB) (Feng et al., 2010; Meng et al., 2003; Ren et al., 2002; Wei et al., 2010). The volcanism occurred over a vast area in the XMOB primarily consisting of granites (Wu et al., 2003a, 2003b). Some hypotheses have been raised to explain the mechanism of Mesozoic volcanism activities and extension, including mantle plume (Qiang et al., 1998), post-orogenic gravity collapse after the continental collision (Fan et al., 2003) and the rollback of Paleopacific plate (Wang et al., 2006) and however, no consensus has been reached (Wang et al., 2006; Wu et al., 2003a). Therefore, detailed three-dimensional crustal velocity structure of NE China is required for understanding the geodynamic process and the mechanism of the late Mesozoic extension and volcanism in NE China.

NE China has been the subject of numerous seismic tomographic studies (Chen and Pei, 2010; Huang, 2003; Lei and Zhao, 2005; Li et al., 2012; Pei and Chen, 2010; Tang et al., 2013; Zheng et al., 2011), but the model resolution was limited by sparse seismic station coverage in the region until the deployment of NECESSArray (NorthEast China Extended Seismic Array). The main objective of the NECESSArray project was to study the crustal and mantle structure of NE China to better understand the complex structure of the subducted slab in the mantle transition zone and its relationship to the extensive magmatism in the region. Upper mantle structure of NE China has been inferred from S wave tomography by Tang et al. (2014) using NECESSArray data and revealed a continuous slow velocity anomaly beneath the Changbaishan volcanoes down to the mantle transition zone. They interpreted it as the subduction related mantle upwelling. Crustal thickness from receiver function study implied that high topography at the flank of the SLB could be dynamically supported by buoyant upper mantle (Tao et al., 2014). However, S-wave velocity structure of crust and uppermost mantle in NE China is still poorly constrained from previous studies. In this study, we construct a high resolution 3-D crustal and uppermost mantle velocity model by joint inversion of ambient noise surface wave dispersion data and receiver function measurements. This study together with previous two studies using NECESSArray data (Tang et al., 2014; Tao et al., 2014) provides further insight into the understanding of geology and tectonic evolution of NE China.

This study comprises two parts: (1) to obtain phase velocity maps from ambient noise tomography (ANT) with periods between 6 s and 40 s by using data recorded by NECESSArray; and (2) to get high resolution three-dimensional S-wave velocity structure of the crust and uppermost mantle beneath NE China by jointly inverting ANT surface wave dispersion measurements and receiver functions.

2. Ambient noise tomography

Seismic data used in this study were recorded by the NECESSArray experiment, a broadband seismic experiment that consisted of 127 stations, with station spacing about 70 km, deployed from $\sim 116^\circ\text{E}$ to $\sim 132^\circ\text{E}$ in longitude and from $\sim 42^\circ\text{N}$ to $\sim 47.5^\circ\text{N}$ in latitude. From September 2009 to August 2011, 120 stations were deployed with an additional 7 stations deployed for 1 yr from September 2010 to August 2011 (blue triangles in Fig. 1). Teleseismic waveforms were also collected from 7 permanent CEA (China Earthquake Administration) stations to obtain P wave receiver functions for joint inversion (black triangles in Fig. 1).

We adopted the similar data processing procedure with that described by Bensen et al. (2007) and Yang et al. (2007) to obtain surface wave dispersion curves from ambient noise. After removing the instrument responses, seismic data were decimated to 1 Hz and processed as daily records at each station. All records were band-pass filtered between 5 s and 150 s, and then we applied

temporal normalization to remove the effects of earthquakes using a weighted running average method. We also applied spectral normalization for each record to avoid significant spectral imbalance and to broaden the bandwidth of the ambient noise (Bensen et al., 2007; Lin et al., 2007). Cross-correlations between all possible station pairs were carried out in the frequency domain. Finally, we stacked 2 yr of correlation sequences of station pairs to obtain the empirical Green functions. Fig. 2a shows an example of a cross-correlation record section between NE79 and other stations. Coherent signals are clear at both positive and negative lag times. The positive and negative components correspond to waves traveling in opposite directions between stations. We followed the same procedure used by Zheng et al. (2011) to remove disturbances induced by Kyushu volcanoes at periods less than 16 s (Zeng and Ni, 2010; Zheng et al., 2011). We calculated Kyushu signal arrival time and only retained positive or negative component of cross-correlation that is free from Kyushu signal disturbance. For periods greater than 18 s, we averaged the positive and negative lag time series to simplify the data and enhance the signal-to-noise ratio (SNR). The SNR is an important indicator for the reliability of ambient noise surface wave measurements. It is defined by Bensen et al. (2007) as the ratio of peak amplitude in the signal window with the RMS (Root Mean Square) level of 500 s noise window that trails the signal window at each period.

We then performed frequency–time analysis with a phase-matched filter applied to measure phase velocity dispersion curves (Levshin and Ritzwoller, 2001). The intrinsic 2π phase ambiguity of phase measurements was resolved using the global phase velocity reference model (Ekström, 2011). The Rayleigh phase dispersion measurements between 6 s and 40 s periods were used to invert for 2-D phase velocity maps on a $0.5^\circ \times 0.5^\circ$ spatial grid across NE China by applying a linear ray theoretic tomographic method (Barmin et al., 2001; Yang et al., 2010). Three criteria were set to select dispersion data for the tomography. First, we discarded dispersion measurements with SNR less than 20 for each period band between 6 s and 40 s. Second, stations should be separated by at least 3 wavelengths for a certain period. Third, measurements should be coherent with each other across the data set, which means that Rayleigh wave phase travel times with misfits larger than 6 s were discarded. Although both finite frequency effects and multi-path effects can affect the results, the influences are generally small. In this study, we only used periods shorter than 40 s and thus ray theoretic tomography should be sufficient (Yang et al., 2007). It is usually difficult to predict uncertainties for surface wave dispersion observations through time–frequency analysis and tomographic inversion (Barmin et al., 2001), so we also employed an eikonal tomography approach (Lin et al., 2009) to obtain surface wave data uncertainties. Surface wave velocity uncertainties are about 5–20 m/s in the center of the study region but increase near its periphery. We set double average uncertainties at each period for regions without station coverage.

Phase velocity maps for periods from 6 s to 40 s are shown in Fig. 3. For short periods from 6 to 12 s (Figs. 3a–3d), Rayleigh wave phase velocities are predominantly sensitive to the upper crust, and especially correlate well with the sedimentary basins and mountain ranges shown in the geological map (Fig. 1). Primary features shown in Figs. 3a–3c are low velocity anomalies in the SLB, the Erlian basin and the Hailaer basin, which are parts of the Mesozoic rift systems in NE China (Ren et al., 2002). A slow anomaly emerges at 8 s period beneath the western part of the XMOB and becomes larger at longer periods, dominating the XMOB till 40 s. At 20 s period, low velocities begin to emerge beneath the CBM. At longer periods between 30 and 40 s (Figs. 3f–3k), the main features in these maps correlate well with crustal thickness variations: high velocities correlate with thin crust beneath the SLB (Tao et al., 2014). The ANT resolution depends on the ray paths and

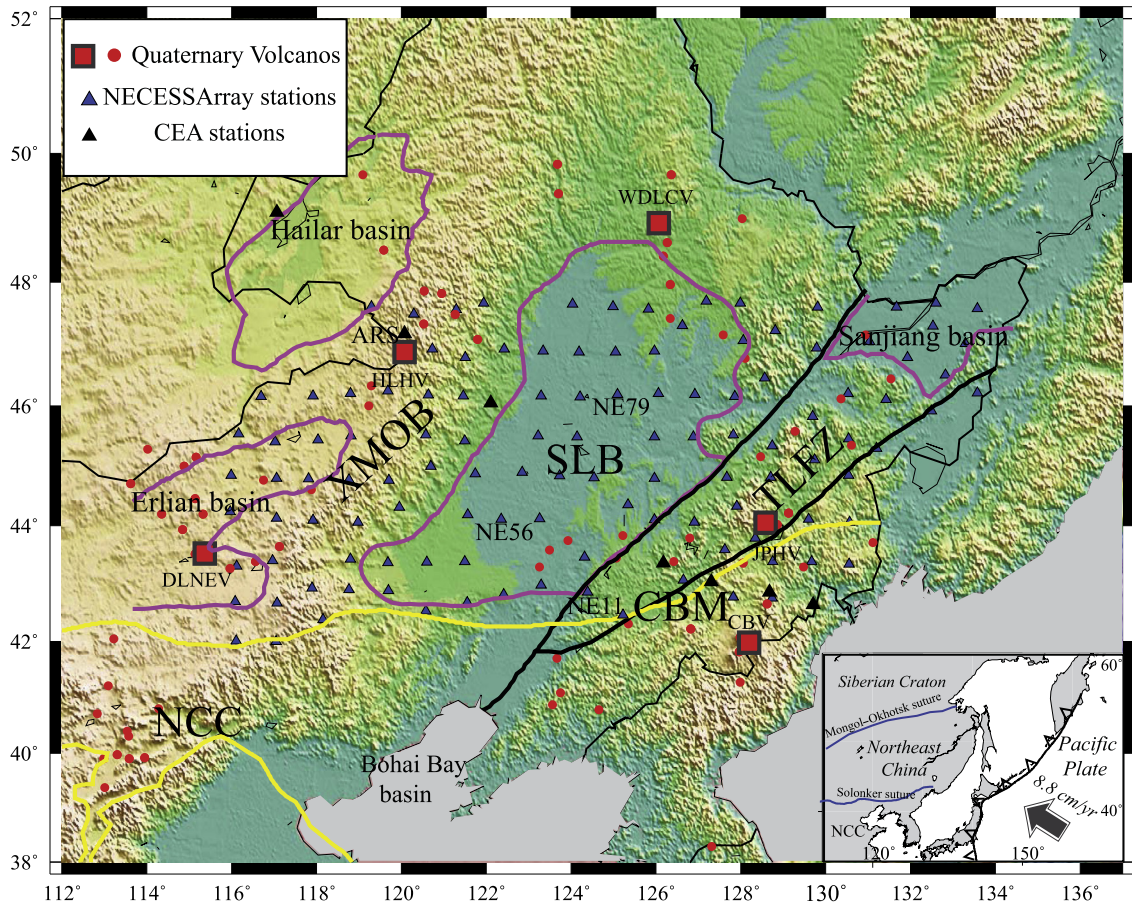


Fig. 1. Tectonic map of Northeast China (NE China) and station distribution. Yellow lines indicate the tectonic boundary of NE China and the North China Craton (NCC). NE China is comprised of the Xing'an–Mongolia orogenic belt (XMOB), the Songliao basin (SLB) and the Changbaishan mountain range (CBM). Other tectonic features are the Tanlu faults zone (TLFZ), Bohai Bay basin, Hailar basin, Sanjiang basin and Erlian basin; red points are the Quaternary volcanoes in the region. CBV: Changbaishan volcanoes; JPHV: Jingpohu volcanoes; WDLCV: Wudalianchi volcanoes; HLHV: Halaha volcanoes; DLNEV: Dalainoer volcanoes. Seismic waveform data are collected from 127 NECESSArray stations (blue triangles), and 7 permanent CEA stations (black triangles). The bottom-right inset shows the motion of the Pacific plate relative to the Eurasia plate. NE79, NE11, NE56 and ARS are seismic stations mentioned in Fig. 2. (For interpretation of the references to color in this figure legend, the reader is referred to the web version of this article.)

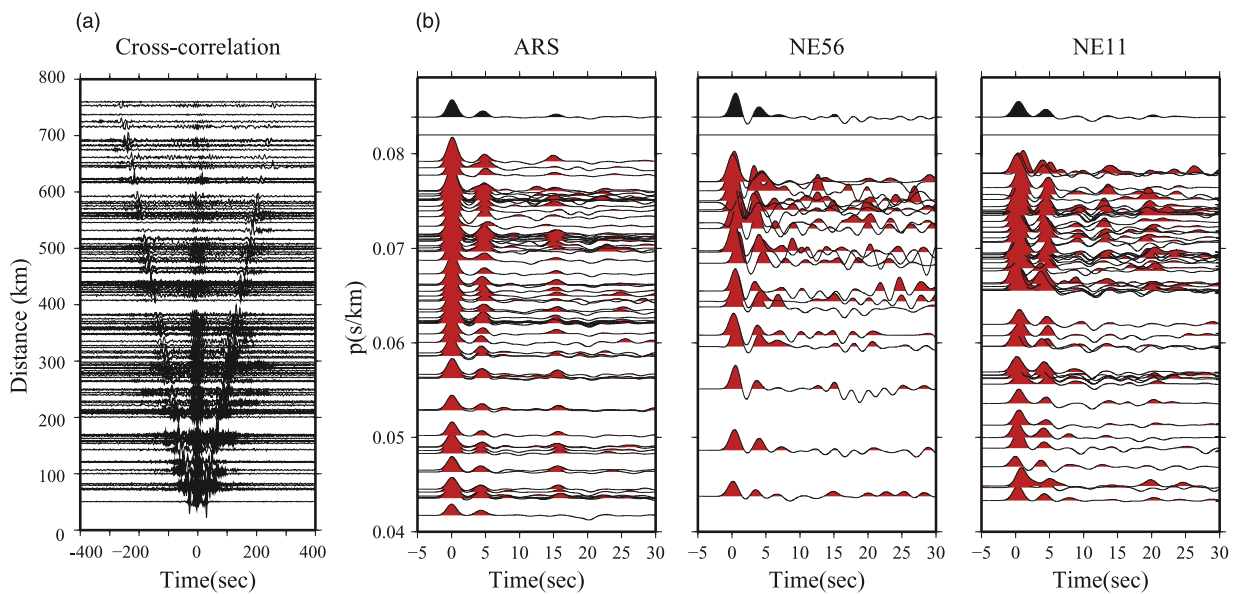


Fig. 2. (a) Example of a cross-correlation record section of NE79 and other stations from 24-month vertical components. (b) Moveout corrected receiver functions (red) recorded at station ARS, NE56 and NE11 in the XMOB, the SLB and the CBM, respectively. The top one is the stacked receiver function for inversion (black). For stations at rock sites (ARS and NE11), clear Moho conversions and multiples are observed. For station in the SLB, Moho multiple phases are masked by basin multiple phases. Locations of these stations are marked in Fig. 1. (For interpretation of the references to color in this figure legend, the reader is referred to the web version of this article.)

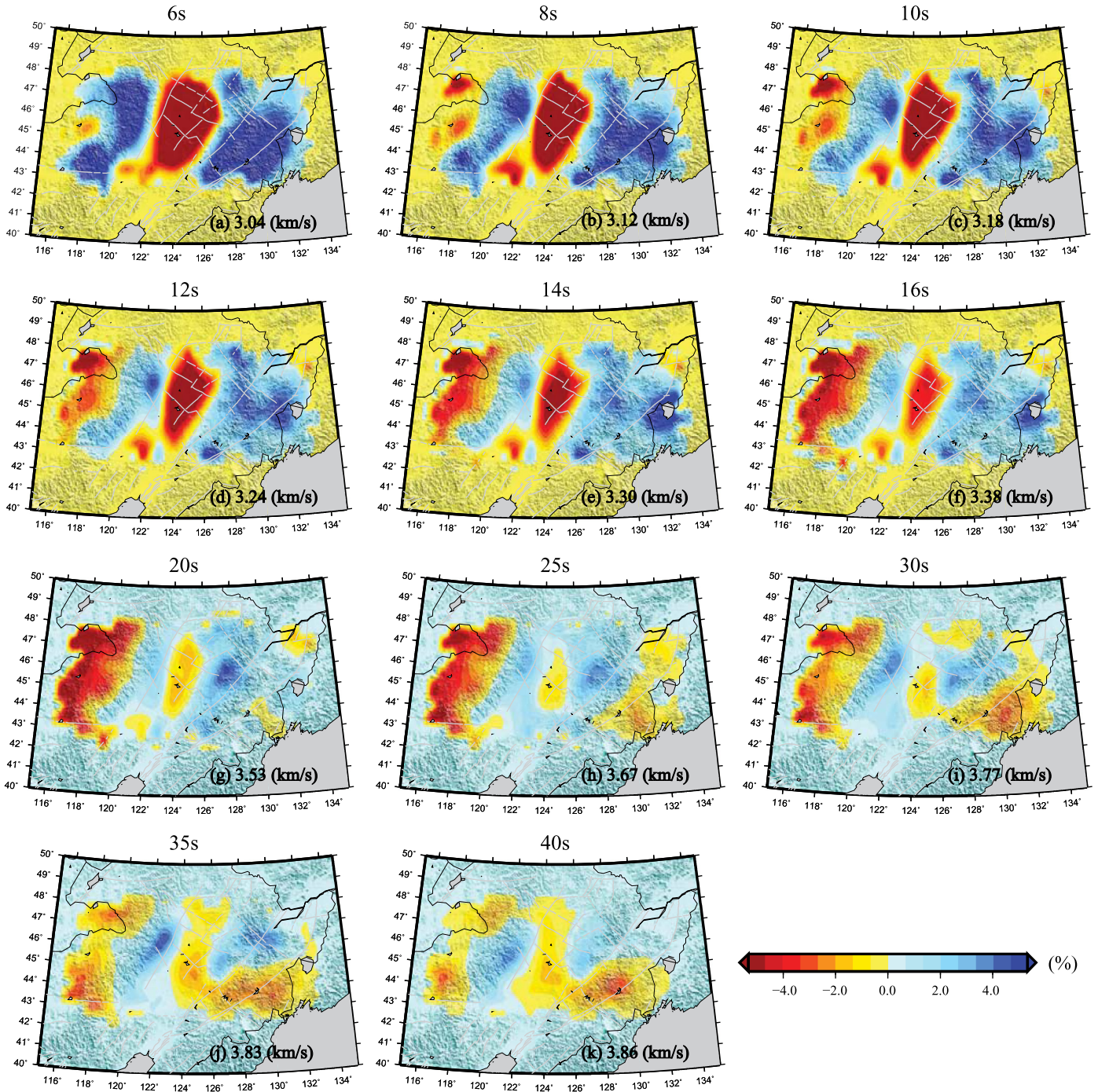


Fig. 3. Phase velocity perturbation maps at periods between 6 s and 40 s with respect to the averaged velocity labeled at the right bottom.

station distribution, parameterization and regularization. We conducted synthetic tests to qualitatively investigate the fidelity of our ambient noise tomography. The checkerboard recovery results are shown in Fig. S1 as supplementary material. For periods between 6 s and 40 s, recovery is reasonably good for areas with dense ray coverage. However, smearing effects still exist at edges.

3. Receiver functions

To obtain reliable receiver functions, we visually selected P waves with high signal-to-noise ratios, epicentral distances between 30° and 90°, and earthquakes of magnitude >5.5 mb. All waveforms were pre-filtered with a band-pass of 0.1–2.5 Hz. Re-

ceiver functions were obtained by deconvolving radial components from vertical components in the time domain using the iterative deconvolution technique (Ligorria and Ammon, 1999). A Gaussian factor of 1.25 in the deconvolution is used to reduce the influence of small-scale effects (Julià et al., 2000). A time window between –5 s and 30 s was chosen to cut receiver functions to retain Moho conversion phases as well as reverberation phases. Erratic traces or outliers were visually removed. Stations with more than 30 receiver functions were retained. After this selection, we obtained 5001 receiver functions from 119 stations of NECESSArray. Finally, we move-out corrected each receiver function for both direct Ps conversion and reverberations to a horizontal slowness of 0.064 s/km (Chen and Niu, 2013) and then stacked them to get

the target receiver function for each station in order to enhance signal-to-noise ratios and suppress signals caused by small-scale heterogeneities, anisotropy or non-plane interfaces. We measured the data uncertainty for a stacked receiver function by calculating standard deviation over all stacking traces. Fig. 2b shows the corrected receiver functions (red curves) aligned according to the ray parameter at station ARS in the northern XMOB, NE56 in the western SLB, and NE11 in the southwestern CBM. The stacked receiver functions were also shown as back curves at the top. Receiver functions from different tectonic regions display significant variations. In the XMOB and CBM (ARS and NE11 in Fig. 2b), receiver functions show clear Moho converted phases and reverberations. While in the SLB (NE56 in Fig. 2b), Moho reverberated phases are hard to discern for most receiver functions and a strong negative signal exists between 2 s and 4 s, which is related to the thick sedimentary layer in this region.

4. Joint inversion method

Surface wave data are sensitive to absolute S-wave velocity at depth and receiver functions provide constraints on velocity contrasts, particularly the crustal thickness. The merits of joint inversion using both datasets have been discussed in numerous previous studies (Bodin et al., 2012; Julià et al., 2000). Different techniques have been developed, such as linear techniques and non-linear techniques (Bailey et al., 2012; Julià et al., 2000; Liu et al., 2014; Tkalčić et al., 2012; Yoo et al., 2007), including the niching genetic algorithm (Lawrence and Shearer, 2006), Bayesian Monte-Carlo method (Bodin et al., 2012; Shen et al., 2013a, 2013b), and so on.

We parameterized the 3-D model of NE China in terms of one-dimensional depth dependent velocity profiles determined at the center of each cell. If a cell contains receiver functions, then two sets of data, receiver functions and phase velocities, were jointly inverted at the center of the cell, otherwise only surface wave data were inverted. The model was parameterized by $0.5^\circ \times 0.5^\circ$ in horizontal dimension, and layer thickness varies from 0.5 km for the first 5 km depth at top, 2.5 km in the upper 40 km depth, 5 km from depth of 40 km to 80 km, and to 10 km to a depth of 150 km. P wave velocities and densities were estimated from a depth-dependent Vp/Vs ratio and empirical relationships, respectively. In this study, we set the Vp/Vs ratio equal to 2.0 in the top 10 layers for the SLB region and the top 5 layers for other basins to represent the sediment, and we took Vp/Vs ratio for each location from the receiver function study (Tao et al., 2014) for upper 40 km in the XMOB and CBM and 30 km in the SLB, and set Vp/Vs ratio as 1.732 for rest layers. We also employed Birch's law of $\alpha = 3.125\rho - 2.40$ (Birch, 1961) to relate the P wave velocity to density.

To integrate the two sets of data, we minimized the following penalty function (Julià et al., 2000; Maceira and Ammon, 2009):

$$\varepsilon = c_1 \|G_s(m) - d_s\|^2 + c_2 \|G_r(m) - d_r\|^2 + \alpha_l \|\Delta m\|^2 + \alpha_v \|Sm\|^2 + \alpha_d \|Dm_a\|^2 \quad (1)$$

where G_s and G_r are matrices containing partial derivatives of the seismic S-wave velocity model for the dispersion and receiver function, respectively. The m is the 3-D S-wave velocity model to be inverted. The d_s and d_r are corresponding data vectors. The c_1 and c_2 are weights for two types of data. Following Julià et al. (2000) and Maceira and Ammon (2009), the c_1 and c_2 are set equal to $\sqrt{p/(N_s\sigma_s^2)}$ and $\sqrt{(1-p)/(N_r\sigma_r^2)}$, respectively. The N_s and N_r are data length for the surface waves and receiver functions respectively. The p value, a weighting factor used to balance the influences of the two datasets in the inversion, is between 0 and 1. After several experiments, we chose 0.6 as the

best tradeoff for the joint inversion. Fig. S2 shows the average misfits for surface wave data and receiver functions as a function of the influence parameter p . The matrix Δ and the corresponding weighting a_l construct the second-order difference between S-wave velocity values in adjacent horizontal cells and ensure the lateral smoothing across the region. The S , a first-order difference roughening matrix, and the smoothing parameter a_v make the model in each column vertically smooth. The diagonal matrix D contains constraint weighting to a priori velocity values in m_a . We started from an averaged 1-D model (Ritzwoller et al., 2002; Shapiro and Ritzwoller, 2002) over the study region with a Q model from PREM (Dziewonski and Anderson, 1981). The σ^2 is the corresponding data uncertainty. Eq. (1) is solved using the LSQR algorithm (Paige and Saunders, 1982).

5. Joint inversion results

We constructed a 3-D S-wave velocity model using the joint inversion of receiver functions and Rayleigh phase velocities from the ambient noise tomography. Fig. 4 shows depth-dependent S-wave velocities at three locations (white points in Fig. 5b) representing three distinct tectonic regions of the XMOB (Figs. 4a, 4b and 4c), the SLB (Figs. 4d, 4e and 4f), and the CBM (Figs. 4g, 4h and 4i), together with associated synthetic and observed receiver functions and dispersion curves, respectively. All surface wave dispersion curves are fit quite well. Moho related phases (Pms and Ppps) of receiver functions are also fit well for locations in the XMOB and CBM. Observed receiver functions are much more complicated at stations with thick sedimentary deposits (Fig. 4e) relative to hard rock sites (Figs. 4b and 4h). Thus, the best fitting model can only recover primary phase arrival times of receiver functions rather than amplitudes for locations in the SLB.

The 3-D S-wave velocity models from joint inversion are presented in Fig. 5 as horizontal slices at different depths from the surface down to 60-km depth. Three vertical cross-sections are also presented in Fig. 6 with their locations shown in Fig. 5a. Fast velocity anomalies in the upper crust are observed beneath the mountain regions (XMOB and CBM) and the SLB is dominated by a strong slow velocity anomaly as shown in Figs. 5a–5c. A slow S-wave velocity anomaly emerges from the western part of the XMOB at a depth of 7.5 km (Fig. 5d) and then expands to the entire orogenic belt within our study area in the mid and lower crust (Figs. 5e–5i and Fig. 6). The three EW transects A–A', B–B' and C–C' in Fig. 6 clearly show the vertical extent of the relatively slow anomaly beneath the XMOB. The horizontal layered slow anomaly is observed throughout the mid-and-lower crust of the XMOB between 10 km and 30 km as shown in Fig. 6. It terminates in the east at the boundary between the SLB and XMOB. Compared with the XMOB, the CBM has relatively fast velocity in the mid-and-lower crust. From 42.5 km to 60 km, corresponding to the uppermost mantle beneath the XMOB and the CBM, the CBM is characterized as slow velocity. Two slow velocity anomalies are also imaged in the southern and northern parts of the XMOB (Figs. 5j–5l), which are roughly beneath two Cenozoic volcanic groups, Halaha volcanoes in the north and Dalainoer volcanoes in the south (Liu et al., 2001), respectively.

We also obtained the Moho depth by measuring the largest velocity gradient in the depth range between 20 and 50 km from our 3-D S-wave velocity model. It is based on the assumption that the Moho is a sharp gradient zone where the S-wave velocity changes most. Figs. S3a and S3b compare the Moho along a NW–SE profile (D–D' in Fig. S3c) from receiver function migration (Fig. S3a) and from velocity gradient of the S-wave velocity model (Fig. S3b). Migration is performed using the 3-D velocity model from this study (Wilson and Aster, 2005). A westward tilting of the Moho beneath the SLB is observed by both methods. Moho depth (Fig. S3c) from

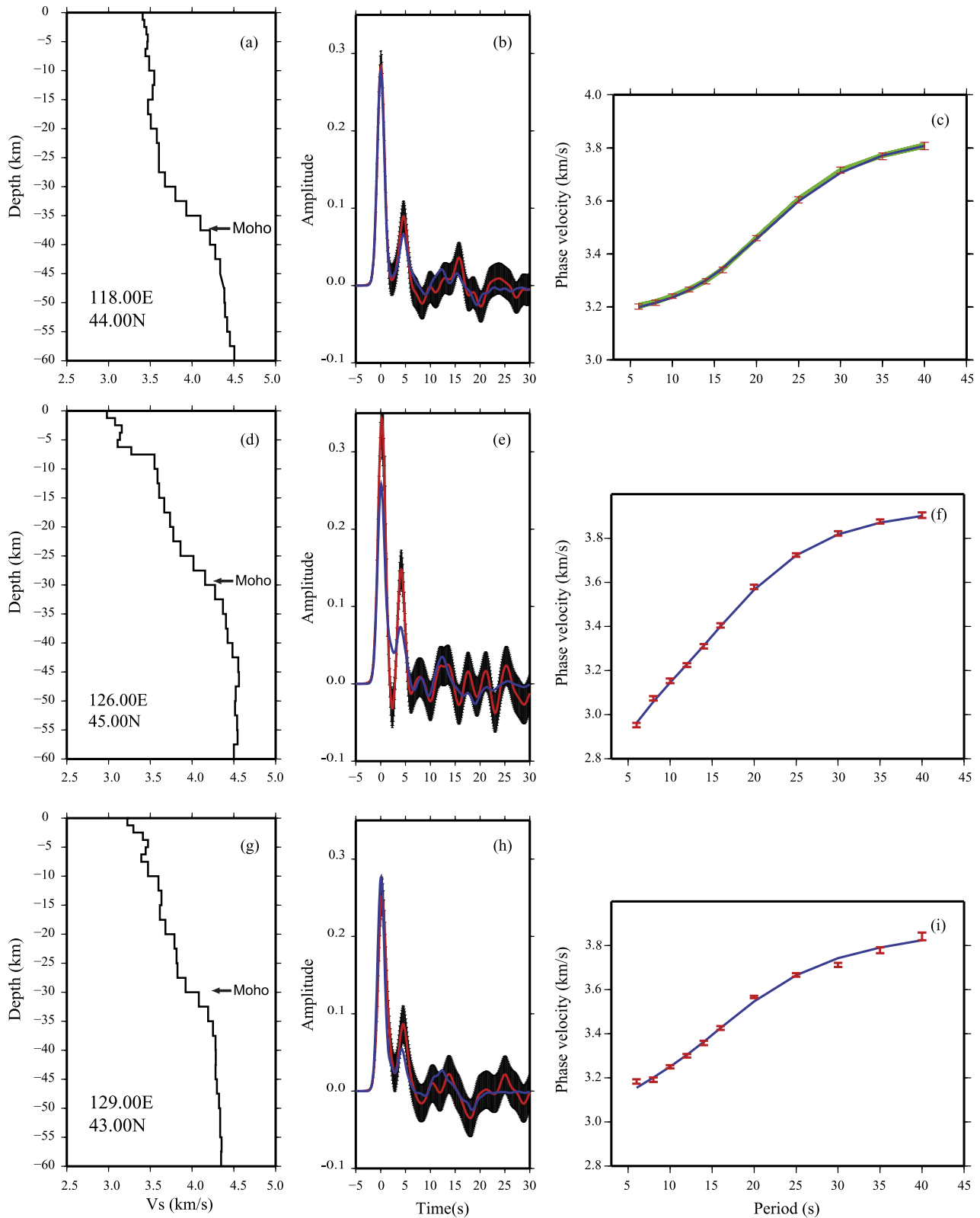


Fig. 4. Joint inversion results from three locations (in Fig. 5b) in the XMOB (a, b and c), the SLB (d, e and f) and the CBM (g, h and i). Observed receiver functions (red lines) with 1σ error bars are plotted with predicted receiver functions (blue lines) in (b), (e) and (h). Observed surface wave dispersion curves (red error bar) are plotted with predicted surface wave dispersion curves (blue lines) from joint inversion in (c), (f) and (i). Best 3000 predicted surface wave dispersion curves from MCMC inversion are also shown in (c) as green lines. Corresponding model ensemble is presented in Fig. S4a. (For interpretation of the references to color in this figure legend, the reader is referred to the web version of this article.)

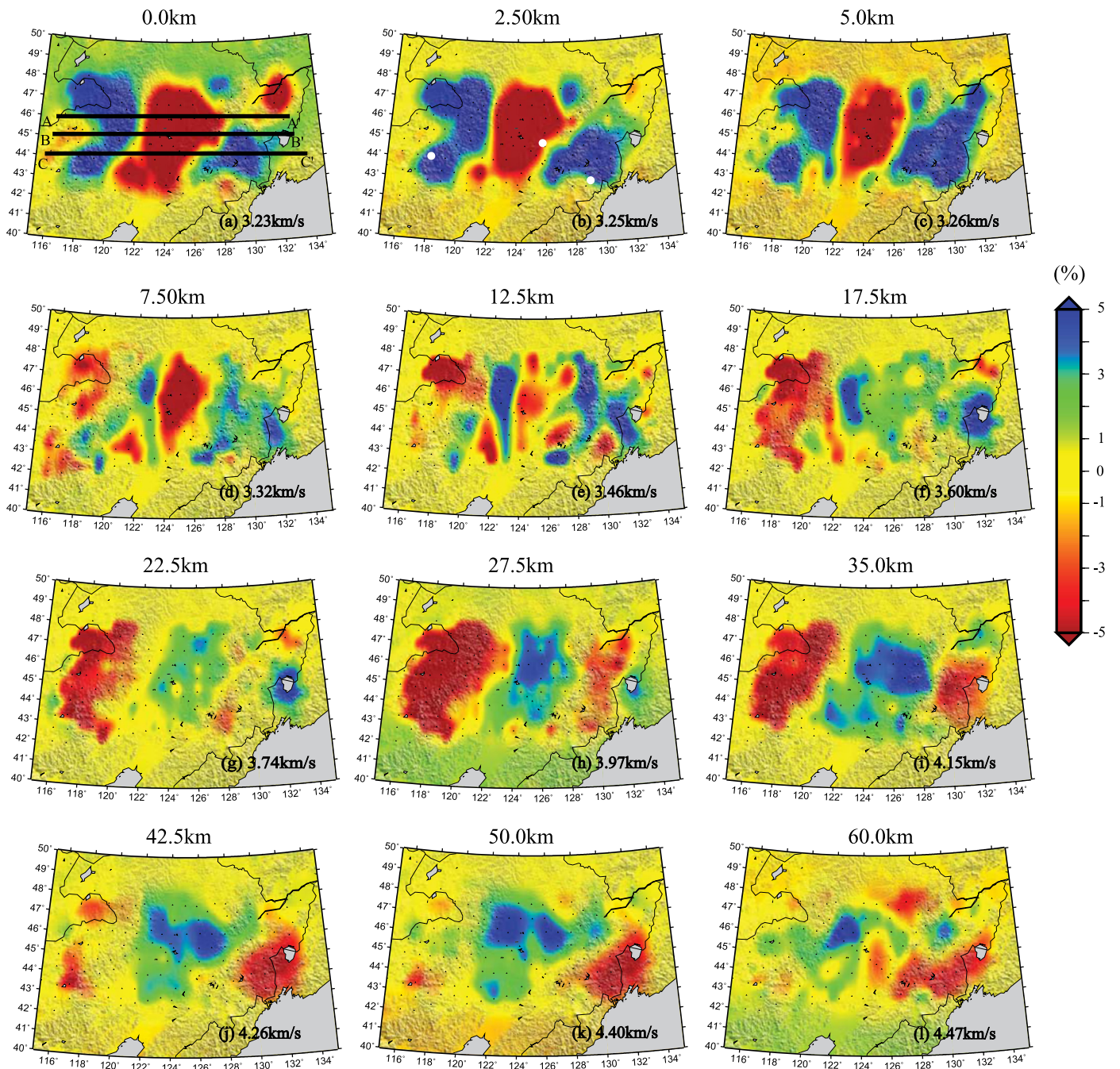


Fig. 5. S-wave velocity model from joint inversion for NE China. Depth slices show velocity variations relative to the averaged velocity of each depth. A–A', B–B' and C–C' in Fig. 6a delineate the positions of the vertical velocity sections shown in Fig. 7. Black triangles are seismic stations. White points in (b) give the locations of 1-D profiles in Fig. 4.

this study and from previous receiver function H–K study (Fig. S3d) (Tao et al., 2014) are quite similar with each other, although differences still exist in areas with poor receiver function fits in the inversion or in areas even without receiver functions, including the SLB and peripheries of the study region. These differences could also be caused by different reference velocity models used (Sun and Toksöz, 2006).

Since the Moho depth information of this study primarily comes from receiver function, its influence on the final velocity model should be tested. Moreover, the joint inversion method adopted in this study does not generate model uncertainties of S-wave velocities. We thus used a Markov chain Monte Carlo (MCMC) method to invert for S wave velocity by only using

surface wave data, and roughly estimated model uncertainties (Afonso et al., 2013; Shen et al., 2013b). This non-linear inversion method generates an ensemble of acceptable models to represent the posterior probability distribution function (PDF) of the earth structure reflected by the observations (Afonso et al., 2013; Bodin et al., 2012; Shen et al., 2013b). We used 4 b-splines and 5 b-splines to represent crustal and mantle layers, respectively. The MCMC inversion started from the same 1-D velocity (Shapiro and Ritzwoller, 2002) to that we used in the joint inversion and was perturbed $\pm 30\%$ as searching bands. The initial value of the Moho depth was taken from the model of Tao et al. (2014). P wave velocity and density are scaled by using the same relationship with the joint inversion. We used a delay rejection adaptive Metropo-

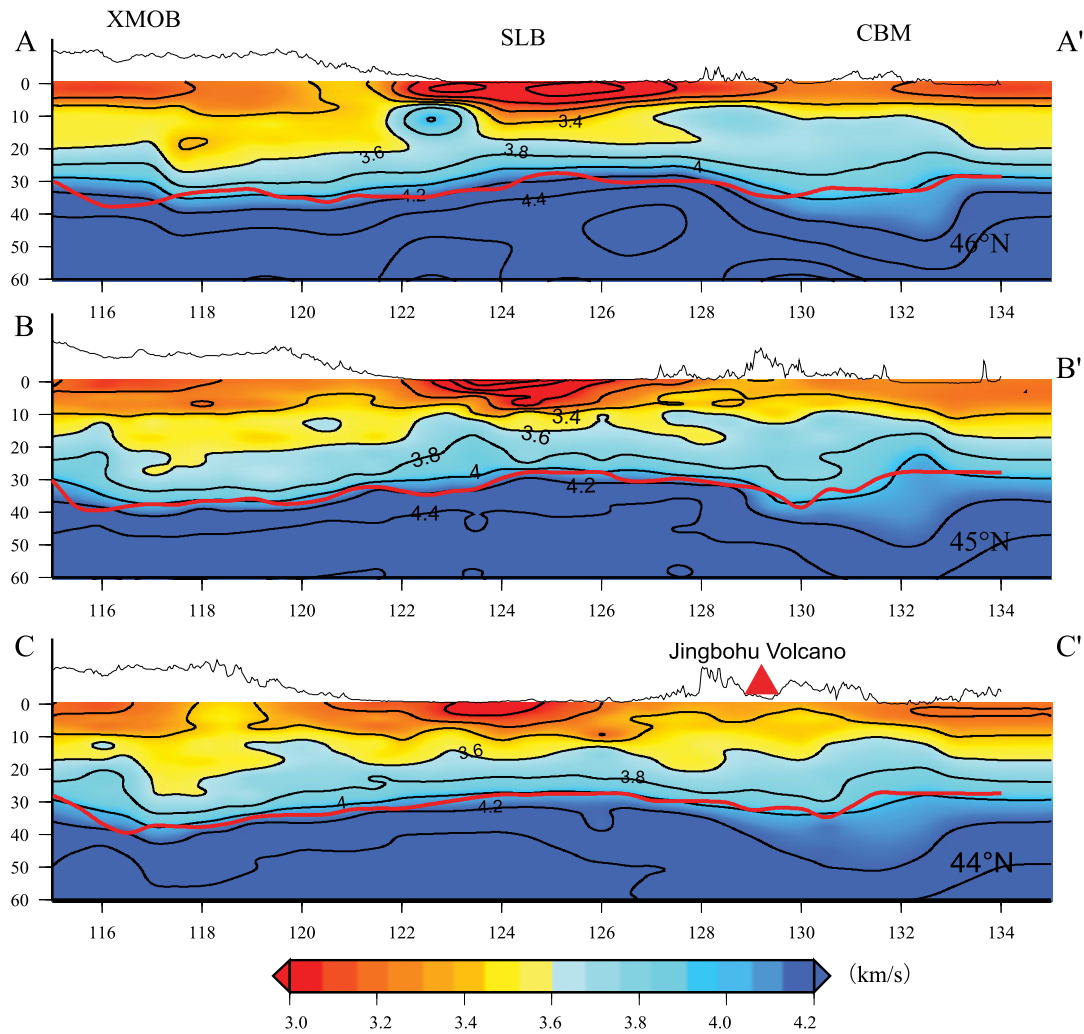


Fig. 6. Vertical sections of absolute S-wave velocity model. Surface topography along the profiles is plotted at the top. Velocity contours are also shown. Jingbohu volcano is marked with red triangles. Red lines are Moho depths from velocity gradient. (For interpretation of the references to color in this figure legend, the reader is referred to the web version of this article.)

lis algorithm to search the model space (Haario et al., 2006) and stored the final 3000 samplings as the model ensemble and calculated uncertainties for each location. Fig. S4a compares the 1D velocity profile at (118°E, 44°N) from joint inversion (blue line) and MCMC (green line), with the predicted 3000 surface wave dispersions shown in Fig. 4c with green lines. Two models are quite similar with each other in the crust and lower part of uppermost mantle in Fig. S4a (also in Figs. S4b and S4c), but obvious difference occurs right beneath the Moho, where the joint inversion model is much smoother than MCMC model. This means that surface wave plays more important role in the joint inversion due to the relatively strong smoothing effects and the model uncertainties from MCMC could be roughly used for the joint inversion model only in the crust and lower part of uppermost mantle. Model uncertainties in the upper crust and lower part of uppermost mantle are slightly larger compared with that in the mid-and-lower crust (<80 m/s) (Figs. S4d–S4f).

6. Discussion

The joint inversion model shows that slow anomaly in the SLB becomes thicker and larger (also seen in Fig. 6) from south to north, which is consistent with previous geological studies (Wei et al., 2010) that the southern and northern parts of the SLB experienced different subsidence histories. The northern SLB began

developing in the Late Jurassic and experienced syn-rift as well as post-rift subsidence. In contrast, the southern SLB only experienced minor post-rift subsidence (Wei et al., 2010). Fig. 7 shows that velocity model at 6.5 km beneath the SLB correlates well with the basin basement determined from previous studies (Feng et al., 2010). The sedimentary fill is thin in the basin margins corresponding to relatively fast velocity. The deposit thickness of the central basin area is nearly 10 km (Feng et al., 2010) and our model shows a strong slow velocity anomaly in this region. In the south, a high velocity zone associated with the “Southwest uplift” separates the slow velocity anomaly beneath the Kailu depression from the central basin. The SLB is known to be composed of several structural domains, such as the western slope, the northern tilted area, the central basin, the northeastern uplift, the southeastern uplift, the southwestern uplift, and the Kailu depression (Feng et al., 2010; Wei et al., 2010). Such complicated structural divisions of SLB and the westward tilted Moho beneath the SLB (Fig. S3) (Tao et al., 2014) might be related to the complex evolution of the SLB since the Late Triassic, including multiple stages of rifting, subsidence, uplift, compression and partial inversion (Song, 1997).

High velocity anomalies are dominant beneath the SLB in the mid-and-lower crust, which probably reflects the mafic intrusions associated with the rifting process (Zhang et al., 2011). In the uppermost mantle, velocity is still high beneath the SLB region.

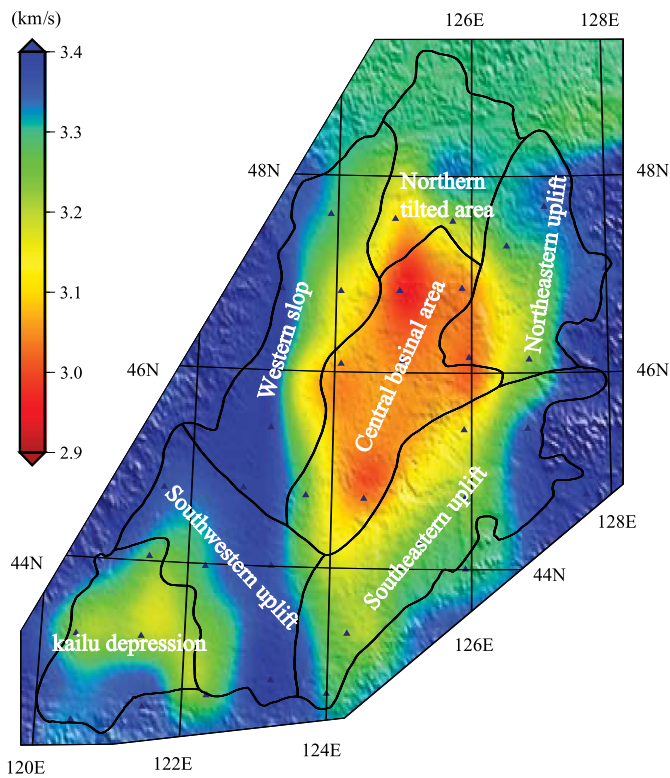


Fig. 7. S-wave velocity model of the SLB at 6.5 km depth. Lines show the basin boundary and major structural domains of the SLB. The thickness of deposits in the central basin is about 10 km (Feng et al., 2010).

A body wave tomographic model from Tang et al. (2014) shows that this high velocity anomaly extends to ~150-km depth. High mantle velocity beneath the SLB was suggested to result from cooling of the lithosphere since rifting ceased about 100 Ma (Wei et al., 2010).

Beneath the CBM, S-wave velocity is generally slow from the lower crust to uppermost mantle (Figs. 5h–5i). Geochemical studies suggest that high degree partial melting might have occurred beneath the Changbaishan volcanoes related to high upper mantle temperature (Chen et al., 2007; Zou et al., 2008). Recently, Tang et al. (2014) obtained a detailed S-wave velocity tomographic model beneath NE China down to 900-km depth using teleseismic data recorded by NECESSArray. They reported that a slow velocity anomaly extends westward from the surface of the Changbaishan volcanoes in the CBM to the mantle transition zone at depth. The slow velocity anomaly is surrounded by fast velocity anomalies in the mantle transition zone inferred to be subducted Pacific slab. The continuous slow anomaly beneath the CBM was interpreted as a local upwelling in response to the slabs sinking into the lower mantle. The upwelling heats up the upper mantle at shallower depths and results in partial melting that feeds the Changbaishan volcanoes (Tang et al., 2014). The observation of uplifted Moho beneath the CBM (Fig. S3) also support the mantle upwelling model (Tao et al., 2014).

Beneath the XMOB, the mid-and-lower crustal velocity is generally slower than other two regions (Figs. 5d–5i). Fig. 8 shows the averaged 1-D S-wave profile beneath the XMOB, the SLB and the CBM. The AK135 model (Kennett et al., 1995) is also presented as a reference. In the mid-and-lower crust, the slowest average velocity is observed beneath the XMOB and it is also slower than the global average AK135 model at those depth ranges. In the uppermost mantle, however, the slowest average velocity occurs beneath the CBM, corresponding to the slow velocity anomaly extending to the mantle transition zone.

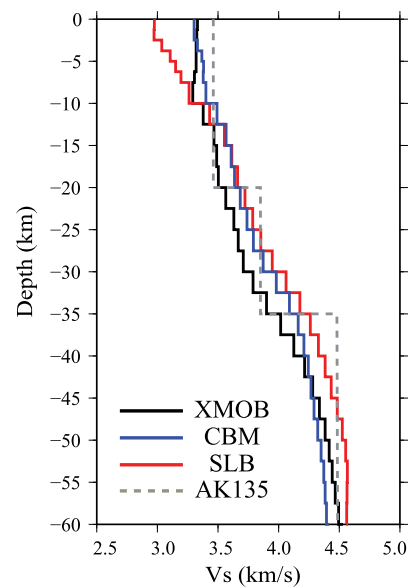


Fig. 8. Average 1D models in the XMOB (black line), the SLB (red line) and the CBM (blue line) compared with AK135 model (gray dashed line). (For interpretation of the references to color in this figure legend, the reader is referred to the web version of this article.)

Relatively slow mid-and-lower crust velocity beneath the XMOB compared to that beneath the CBM cannot be directly attributed to high temperature in the region, considering the low heat flow observations in the XMOB (Tao and Shen, 2008). Also, the CBM experienced more extensive volcanism in the Cenozoic than the XMOB while volcanic eruptions in the XMOB mainly occurred in the Halaha and Dalainoer volcanoes during the Miocene (Liu et al., 2001), which are located in the eastern and western parts of the XMOB. One possible explanation is that the mid-and-lower crust of XMOB is more granitic in composition than the other regions and the global average. The XMOB is characterized by large-scale Mesozoic magmatism, which is dominantly granitic as observed at the surface. Granitic rocks with several kilometers thick cover most part of the XMOB (Wu et al., 2003a, 2003b). Extensive granitic magmas formed during the assembling of continental blocks in the late Paleozoic (Wu et al., 2003b). From 180 to 120 Ma, more granitic rocks were generated probably due to the flat subduction of the Paleo-Pacific plate beneath the NE China (Wang et al., 2006; Zhou and Wilde, 2013). Around approximately 157 Ma, the Paleo-Pacific began to roll back and caused extension, which formed Mesozoic basins including the SLB (Meng, 2003).

Geochemical and isotopic data indicate that the granitic rocks were generated from partial melting of juvenile lower crustal material (Wu et al., 2003a, 2003b). These magmas rose into the upper-and-mid crust making the upper-and-mid crust more silicic and left the lower crust as more mafic. If this is the case, our observation of slower velocity in the lower crust of the XMOB indicates that the XMOB must have lost the mafic part of the lower crust as has been proposed to occur elsewhere (Ducea and Saleeby, 1998). The lack of a very mafic lower crust beneath the XMOB is also supported by the relatively low V_p/V_s ratios beneath the XMOB observed by Tao et al. (2014). The average V_p/V_s ratio beneath the XMOB is about 1.748, corresponding to a Poisson's ratio of 0.257. According to Zandt and Ammon (1995), low crustal average Poisson's ratio (~0.25), is evidence of a predominantly felsic composition in the whole crust and absence of mafic lower crust. We speculate on two possible scenarios for the removal of the mafic lower crust: it could have been removed during the accretion of continental blocks with subsequent delamination during the Paleozoic collisional event or it could be related to

the erosion by convective mantle flow induced by the rollback of the Paleo-Pacific during the middle Mesozoic (Wang et al., 2006; Wu et al., 2003b).

7. Conclusion

In this study, we simultaneously inverted surface wave dispersion measurements derived from ambient noise and teleseismic P-wave receiver functions using data collected by the NECESSArray to obtain a high resolution crustal and uppermost mantle S-wave velocity model of NE China. Rayleigh wave phase velocity maps from 6 s to 40 s are constructed by cross-correlation of 2 yr of continuous ambient noise data recorded by NECESSArray. The 3-D S-wave velocity model from our joint inversion shows good agreement between the crustal velocity structures and surface geology and tectonics in the region. In the shallow crust, slow S-wave velocities are related to the Mesozoic rifting basins in NE China including SLB, Erlian basin, Hailaer basin and Sanjiang basin. High S-wave velocities are correlated with the mountain ranges such as the XMOB and CBM. A high velocity zone in the SLB corresponding to the Southwest uplift separates the SLB into two parts and the southern sub-basin correlates with the Kailu depression. Slow anomalies in the lower crust and uppermost mantle beneath the CBM could be the mantle upwelling from the transition zone as revealed by the recent S mantle model of the NECESSArray (Tang et al., 2014). Beneath the SLB, we observed a high velocity anomaly which is in agreement with the thick and intact mantle lid that is imaged by teleseismic S-wave tomography. Finally, slower velocities in the mid-and-lower crust beneath the XMOB were observed. We interpret the slow velocity in the mid-and-lower crust, as well as relatively low average crustal V_p/V_s ratios (Tao et al., 2014; Zandt and Ammon, 1995), as evidence of a felsic composition beneath the XMOB, which could be the consequence of removal of mafic lower crust in this region. We speculate that the removal of mafic lower crust beneath the XMOB might be due to continental collision in the late Paleozoic or convective removal induced by the rollback of the shallow subducted Paleo-Pacific slab during the middle of the Mesozoic.

Acknowledgements

We thank all the people who had participated in the field work installing/dismantling and servicing the 127 portable seismic stations of the NECESSArray. This study of joint inversion is supported by NSFC grants (40821062; 90814002) and MOST grant (2009AA0934) in China. This is contribution 578 from the ARC Centre of Excellence for Core to Crust Fluid Systems (<http://www.ccfsc.mq.edu.au>) and 985 in the GEMOC Key Centre (<http://www.gemoc.mq.edu.au>).

Appendix A. Supplementary material

Supplementary material related to this article can be found online at <http://dx.doi.org/10.1016/j.epsl.2015.01.044>.

References

- Afonso, J.C., Fullea, J., Griffin, W.L., Yang, Y., Jones, A.G., Connolly, J.A.D., O'Reilly, S.Y., 2013. 3-D multiobservable probabilistic inversion for the compositional and thermal structure of the lithosphere and upper mantle. I: a priori petrological information and geophysical observables. *J. Geophys. Res., Solid Earth* 118 (5), 2586–2617.
- Bailey, I.W., Miller, M.S., Liu, K., Levander, A., 2012. VS and density structure beneath the Colorado Plateau constrained by gravity anomalies and joint inversions of receiver function and phase velocity data. *J. Geophys. Res.* 117 (B2).
- Barmin, M.P., Ritzwoller, M.H., Levshin, A.L., 2001. A fast and reliable method for surface wave tomography. *Pure Appl. Geophys.* 158 (8), 1351–1375.
- Bensen, G.D., Ritzwoller, M.H., Barmin, M.P., Levshin, A.L., Lin, F., Moschetti, M.P., Shapiro, N.M., Yang, Y., 2007. Processing seismic ambient noise data to obtain reliable broad-band surface wave dispersion measurements. *Geophys. J. Int.* 169 (3), 1239–1260.
- Birch, F., 1961. The velocity of compressional waves in rocks to 10 kilobars: 2. *J. Geophys. Res.* 66 (7), 2199–2224.
- Bodin, T., Sambridge, M., Tkalčić, H., Arroucau, P., Gallagher, K., Rawlinson, N., 2012. Transdimensional inversion of receiver functions and surface wave dispersion. *J. Geophys. Res.* 117 (B2).
- Chen, Y., Niu, F., 2013. Ray-parameter based stacking and enhanced pre-conditioning for stable inversion of receiver function data. *Geophys. J. Int.* 194 (3), 1682–1700.
- Chen, Y.J., Pei, S., 2010. Tomographic structure of East Asia: II. Stagnant slab above 660 km discontinuity and its geodynamic implications. *Earthquake Sci.* 23 (6), 613–626.
- Chen, Y., Zhang, Y., Graham, D., Su, S., Deng, J., 2007. Geochemistry of Cenozoic basalts and mantle xenoliths in Northeast China. *Lithos* 96 (1–2), 108–126.
- Ducea, M., Saleeby, J., 1998. A case for delamination of the deep batholithic crust beneath the Sierra Nevada, California. *Int. Geol. Rev.* 40 (1), 78–93.
- Dziewonski, A.M., Anderson, D.L., 1981. Preliminary reference Earth model. *Phys. Earth Planet. Inter.* 25 (4), 297–356.
- Ekström, G., 2011. A global model of Love and Rayleigh surface wave dispersion and anisotropy, 25–250 s. *Geophys. J. Int.* 187 (3), 1668–1686.
- Fan, W., Guo, F., Wang, Y., Lin, G., 2003. Late Mesozoic calc-alkaline volcanism of post-orogenic extension in the northern Da Hinggan Mountains, northeastern China. *J. Volcanol. Geotherm. Res.* 121 (1–2), 115–135.
- Feng, Z., Jia, C., Xie, X., Zhang, S., Feng, Z., Cross, T.A., 2010. Tectonostratigraphic units and stratigraphic sequences of the nonmarine Songliao basin, northeast China. *Basin Res.* 22 (1), 79–95.
- Haario, H., Laine, M., Mira, A., Saksman, E., 2006. DRAM: efficient adaptive MCMC. *Stat. Comput.* 16 (4), 339–354.
- Huang, Z., 2003. Rayleigh wave tomography of China and adjacent regions. *J. Geophys. Res.* 108 (B2).
- Juliá, J., Ammon, C.J., Herrmann, R.B., Correig, A.M., 2000. Joint inversion of receiver function and surface wave dispersion observations. *Geophys. J. Int.* 143 (1), 99–112.
- Kennett, B.L.N., Engdahl, E.R., Buland, R., 1995. Constraints on seismic velocities in the Earth from traveltimes. *Geophys. J. Int.* 122 (1), 108–124.
- Lawrence, J.F., Shearer, P.M., 2006. A global study of transition zone thickness using receiver functions. *J. Geophys. Res.* 111 (B6).
- Lei, J., Zhao, D., 2005. P-wave tomography and origin of the Changbai intraplate volcano in Northeast Asia. *Tectonophysics* 397 (3–4), 281–295.
- Levshin, A.L., Ritzwoller, M.H., 2001. Automated detection, extraction, and measurement of regional surface waves. In: Levshin, A., Ritzwoller, M. (Eds.), *Monitoring the Comprehensive Nuclear-Test-Ban Treaty: Surface Waves*. Birkhäuser, Basel, pp. 1531–1545.
- Li, Y., Wu, Q., Pan, J., Sun, L., 2012. S-wave velocity structure of northeastern China from joint inversion of Rayleigh wave phase and group velocities. *Geophys. J. Int.* 190 (1), 105–115.
- Ligorria, J.P., Ammon, C.J., 1999. Iterative deconvolution and receiver-function estimation. *Bull. Seismol. Soc. Am.* 89 (5), 1395–1400.
- Lin, F., Ritzwoller, M.H., Townend, J., Bannister, S., Savage, M.K., 2007. Ambient noise Rayleigh wave tomography of New Zealand. *Geophys. J. Int.* 170 (2), 649–666.
- Lin, F., Ritzwoller, M.H., Snieder, R., 2009. Eikonal tomography: surface wave tomography by phase front tracking across a regional broad-band seismic array. *Geophys. J. Int.* 177 (3), 1091–1110.
- Liu, J., Han, J., Fyfe, W.S., 2001. Cenozoic episodic volcanism and continental rifting in northeast China and possible link to Japan Sea development as revealed from K–Ar geochronology. *Tectonophysics* 339 (3–4), 385–401.
- Liu, Q., van der Hilst, R.D., Li, Y., Yao, H., Chen, J., Guo, B., Qi, S., Wang, J., Huang, H., Li, S., 2014. Eastward expansion of the Tibetan Plateau by crustal flow and strain partitioning across faults. *Nat. Geosci.* 7 (5), 361–365.
- Maceira, M., Ammon, C.J., 2009. Joint inversion of surface wave velocity and gravity observations and its application to central Asian basins shear velocity structure. *J. Geophys. Res.* 114 (B2).
- Meng, Q., 2003. What drove late Mesozoic extension of the northern China–Mongolia tract? *Tectonophysics* 369 (3–4), 155–174.
- Meng, Q., Hu, J., Jin, J., Zhang, Y., Xu, D., 2003. Tectonics of the late Mesozoic wide extensional basin system in the China–Mongolia border region. *Basin Res.* 15 (3), 397–415.
- Paige, C.C., Saunders, M.A., 1982. LSQR: an algorithm for sparse linear equations and sparse least squares. *ACM Trans. Math. Softw.* 8 (1), 43–71.
- Pei, S., Chen, Y.J., 2010. Tomographic structure of East Asia: I. No fast (slab) anomalies beneath 660 km discontinuity. *Earthquake Sci.* 23 (6), 597–611.
- Qiang, L., Wenchun, G., Deyou, S., Fuyuan, W., Won, C.K., Min, K.D., Jin, M.S., Wonlee, M., Swon, C.S., Yun, S.H., 1998. Tectonic significance of Mesozoic volcanic rocks in northeastern China. *Chin. J. Geol.*, 129–139.
- Ren, J., Tamaki, K., Li, S., Zhang, J., 2002. Late Mesozoic and Cenozoic rifting and its dynamic setting in Eastern China and adjacent areas. *Tectonophysics* 344 (3–4), 175–205.

- Ritzwoller, M.H., Shapiro, N.M., Barmin, M.P., Levshin, A.L., 2002. Global surface wave diffraction tomography. *J. Geophys. Res., Solid Earth* 107 (B12), 2335.
- Sengor, A.M.C., Natal'in, B.A., Burtman, V.S., 1993. Evolution of the Altaid tectonic collage and Palaeozoic crustal growth in Eurasia. *Nature* 364 (6435), 299–307.
- Shapiro, N.M., Ritzwoller, M.H., 2002. Monte-Carlo inversion for a global shear-velocity model of the crust and upper mantle. *Geophys. J. Int.* 151 (1), 88–105.
- Shen, W., Ritzwoller, M.H., Schulte-Pelkum, V., 2013a. A 3-D model of the crust and uppermost mantle beneath the Central and Western US by joint inversion of receiver functions and surface wave dispersion. *J. Geophys. Res., Solid Earth* 118 (1), 262–276.
- Shen, W., Ritzwoller, M.H., Schulte Pelkum, V., Lin, F., 2013b. Joint inversion of surface wave dispersion and receiver functions: a Bayesian Monte-Carlo approach. *Geophys. J. Int.* 192 (2), 807–836.
- Song, T., 1997. Inversion styles in the Songliao basin (northeast China) and estimation of the degree of inversion. *Tectonophysics* 283 (1–4), 173–188.
- Sun, Y., Toksöz, M.N., 2006. Crustal structure of China and surrounding regions from P wave traveltimes tomography. *J. Geophys. Res.* 111 (B3).
- Tang, Y., Chen, Y.J., Zhou, S., Ning, J., Ding, Z., 2013. Lithosphere structure and thickness beneath the North China Craton from joint inversion of ambient noise and surface wave tomography. *J. Geophys. Res., Solid Earth* 118 (5), 2333–2346.
- Tang, Y., Obayashi, M., Niu, F., Grand, S.P., Chen, Y.J., Kawakatsu, H., Tanaka, S., Ning, J., Ni, J.F., 2014. Changbaishan volcanism in northeast China linked to subduction-induced mantle upwelling. *Nat. Geosci.* 7 (6), 470–475.
- Tao, W., Shen, Z., 2008. Heat flow distribution in Chinese continent and its adjacent areas. *Prog. Nat. Sci.* 18 (7), 843–849.
- Tao, K., Niu, F., Ning, J., Chen, Y.J., Grand, S., Kawakatsu, H., Tanaka, S., Obayashi, M., Ni, J., 2014. Crustal structure beneath NE China imaged by NECESSArray receiver function data. *Earth Planet. Sci. Lett.* 398, 48–57.
- Tkalčić, H., Rawlinson, N., Arroucau, P., Kumar, A., Kennett, B.L.N., 2012. Multistep modelling of receiver-based seismic and ambient noise data from WOMBAT array: crustal structure beneath southeast Australia. *Geophys. J. Int.* 189 (3), 1680–1700.
- Wang, F., Zhou, X., Zhang, L., Ying, J., Zhang, Y., Wu, F., Zhu, R., 2006. Late Mesozoic volcanism in the Great Xing'an Range (NE China): timing and implications for the dynamic setting of NE Asia. *Earth Planet. Sci. Lett.* 251 (1–2), 179–198.
- Wei, H., Liu, J.L., Meng, Q., 2010. Structural and sedimentary evolution of the southern Songliao Basin, northeast China, and implications for hydrocarbon prospectivity. *Am. Assoc. Pet. Geol. Bull.* 94 (4), 533–566.
- Wilson, D., Aster, R., 2005. Seismic imaging of the crust and upper mantle using regularized joint receiver functions, frequency–wave number filtering, and multimode Kirchhoff migration. *J. Geophys. Res., Solid Earth* 110 (B5), B05305.
- Wu, F., Jahn, B., Wilde, S.A., Lo, C., Yui, T., Lin, Q., Ge, W., Sun, D., 2003a. Highly fractionated I-type granites in NE China (I): geochronology and petrogenesis. *Lithos* 66 (3–4), 241–273.
- Wu, F., Jahn, B., Wilde, S.A., Lo, C., Yui, T., Lin, Q., Ge, W., Sun, D., 2003b. Highly fractionated I-type granites in NE China (II): isotopic geochemistry and implications for crustal growth in the Phanerozoic. *Lithos* 67 (3–4), 191–204.
- Wu, F.Y., Sun, D.Y., Jahn, B.M., Wilde, S., 2004. A Jurassic garnet-bearing granitic pluton from NE China showing tetrad REE patterns. *J. Asian Earth Sci.* 23 (5), 731–744.
- Xiao, W., Windley, B.F., Hao, J., Zhai, M., 2003. Accretion leading to collision and the Permian Solonker suture, Inner Mongolia, China: termination of the central Asian orogenic belt. *Tectonics* 22 (6), 1069.
- Yang, Y., Ritzwoller, M.H., Levshin, A.L., Shapiro, N.M., 2007. Ambient noise Rayleigh wave tomography across Europe. *Geophys. J. Int.* 168 (1), 259–274.
- Yang, Y., Zheng, Y., Chen, J., Zhou, S., Ceylan, S., Sandvol, E., Tilmann, F., Priestley, K., Hearn, T.M., Ni, J.F., Brown, L.D., Ritzwoller, M.H., 2010. Rayleigh wave phase velocity maps of Tibet and the surrounding regions from ambient seismic noise tomography. *Geochem. Geophys. Geosyst.* 11 (8).
- Yoo, H.J., Herrmann, R.B., Cho, K.H., Lee, K., 2007. Imaging the three-dimensional crust of the Korean Peninsula by joint inversion of surface-wave dispersion and teleseismic receiver functions. *Bull. Seismol. Soc. Am.* 97 (3), 1002–1011.
- Zandt, G., Ammon, C.J., 1995. Continental crust composition constrained by measurements of crustal Poisson's ratio. *Nature* 374 (6518), 152–154.
- Zeng, X., Ni, S., 2010. A persistent localized microseismic source near the Kyushu Island, Japan. *Geophys. Res. Lett.* 37 (24).
- Zhang, F.Q., Chen, H.L., Yu, X., Dong, C.W., Yang, S.F., Pang, Y.M., Batt, G.E., 2011. Early Cretaceous volcanism in the northern Songliao Basin, NE China, and its geodynamic implication. *Gondwana Res.* 19 (1), 163–176.
- Zheng, Y., Shen, W., Zhou, L., Yang, Y., Xie, Z., Ritzwoller, M.H., 2011. Crust and uppermost mantle beneath the North China Craton, northeastern China, and the Sea of Japan from ambient noise tomography. *J. Geophys. Res.* 116 (B12).
- Zhou, J., Wilde, S.A., 2013. The crustal accretion history and tectonic evolution of the NE China segment of the Central Asian Orogenic Belt. *Gondwana Res.* 23 (4), 1365–1377.
- Zou, H., Fan, Q., Yao, Y., 2008. U–Th systematics of dispersed young volcanoes in NE China: asthenosphere upwelling caused by piling up and upward thickening of stagnant Pacific slab. *Chem. Geol.* 255 (1–2), 134–142.